

Internal Solitary Waves in the Mozambique Channel: Observations and Interpretation

J. C. B. da Silva^a, A. L. New^b, J. M. Magalhaes^a

^aUniversity of Lisbon, Institute of Oceanography & Dept. Geographic Engineering,
Geophysics and Energy, Rua Ernesto de Vasconcelos, Campo Grande, 1749-016

Lisboa, Portugal

Telephone: 351 21 750 0312, Fax: 351 21 750 0009

^bOcean Modelling and Forecasting Group, National Oceanography Centre,

Southampton, European Way, Southampton SO14 3ZH, UK

Telephone: 44 2380 596173, Fax: 44 2380 596204

Email addresses:

Corresponding author: jdasilva@fc.ul.pt

Co-authors: anw@noc.soton.ac.uk ; jmagalhaes@fc.ul.pt

Submitted 15 September 2008

Revised 11 February 2009, Journal of Geophysical Research

Abstract

This paper presents new results showing that the Sofala shelf in the Mozambique Channel (20 °S, 36 °E) is a previously unknown “hot-spot” for the generation of internal tides and internal waves. We investigate available ENVISAT ASAR imagery of the region, which is capable of showing the surface signatures of the internal waves. This is complemented by modelling of the ray pathways of internal tidal energy propagation, and of the Baines (1982) barotropic body force which drives the generation of internal tides near the shelf break. The hotspot region is localised between 20-21 °S because of the particular nature of the bathymetry there. Further north and south, the forcing is reduced and insufficient to generate ISWs in the SAR images. The analysis reveals two distinct types of internal wave trains which are observed travelling oceanwards away from the shelf break, and we suggest that these result from, respectively, direct generation at the shelf break, and from “local” generation at about 80 km from the shelf break, due to the surfacing of internal tidal rays at the thermocline. Finally, we have investigated seasonal differences in the wave patterns, which penetrate more extensively into the channel during the southern summer, and appear slightly further to the south during the southern winter. We also conclude that the local generation process is more likely to occur during the winter when the stratification is reduced.

1. Introduction

Internal waves are now viewed as an important mixing mechanism in the world’s ocean, not only for the role they play in deep-ocean mixing (Garrett and St Laurent, 2002), but also for mixing at the base of the mixed layer and in the seasonal thermocline (Moum et al., 2003). In the former case, internal waves may be generated by tidal flow, mean flow, or eddies, interacting with deep ocean topography. While uncertainties still exist over the relative importance of the various mechanisms involved, the breaking of these internal waves may mix the water masses up to mid-depth in some ocean basins (e.g. in the Indian Ocean, New et al.

2007). On the other hand, mixing near the surface affects the properties of those water masses which define the exchanges of heat and freshwater between the atmosphere and ocean. The importance of such mixing in the seasonal thermocline has been strikingly illustrated by Moun et al. (2003), who observed Kelvin-Helmholtz billows leading to turbulence in internal solitary waves (ISWs) over the Oregon continental shelf. In their study it was also shown that ISWs may be continually triggering instabilities as they propagate over the shelf, well before approaching a breaking point in the near shore. Therefore, a significant proportion of the ISW's energy may be lost as it propagates on shore over the shelf. Furthermore, observations of upper ocean ISWs in deep water in the Western Equatorial Pacific also indicate they may be highly turbulent (Pinkel, 2000), and Pingree et al. (1986) showed that mixing from internal tides and waves is important for biological productivity over the Celtic shelf break in the Bay of Biscay. These facts point to the significant role that internal waves may play in near-surface mixing, and it is therefore important to gain knowledge of which areas of the world's oceans have high levels of internal wave activity, and of the mechanisms by which they are formed. Satellite Synthetic Aperture Radars (SARs) are very efficient sensors to explore regions not yet surveyed in detail for the presence of such ISWs, and this paper contributes to the knowledge of where and how ISWs are generated in the Mozambique Channel of the Indian Ocean.

The interaction of the barotropic tide with steep shelf break topography may often result in the generation of large internal waves of tidal period, known as internal (baroclinic) tides (ITs). Internal tidal energy generated at the shelf break may radiate away either horizontally in the form of interfacial ITs on the thermocline, or as "rays" into the stratified continuum below. Consequently, large "interfacial" ITs may form in the thermocline directly above the shelf break, and these, through non-linear evolution, lead to the generation of packets of higher frequency ISWs that can be observed either in situ or in SAR images. On the other hand, the IT energy which propagates downwards into the deep ocean may give rise to a second generation mechanism known as "local generation" (New and Pingree, 1990, 1992; New and Pingree, 2000; Gerkema, 2001; New and da Silva, 2002; Zhao et al., 2004; Akylas et al., 2007; da Silva et al., 2007). Here, a beam or ray of internal tidal energy is generated at "critical" slope regions

of the shelf break where the bottom topographic slope matches the slope of the ray paths, and propagates at an angle to the vertical into the deep ocean interior (see equation 1). These rays reflect from the sea-floor (Pingree and New, 1989, 1991), and interact with the thermocline from below (New and Pingree, 1990), causing large IT oscillations there, and “locally” generating ISWs (i.e. far from the generating shelf break). For the northern Bay of Biscay, this results in a bi-modal distribution of ISW packets, resulting from the “direct” generation mechanism near the shelf break and from “local” generation some 150 km into the ocean (New and Pingree, 1992; New and da Silva, 2002). The local generation mechanism has also been found to be operative in the southern Bay of Biscay by Azevedo et al. (2006), and at the Mascarene Ridge in the Indian Ocean (a region not far from the Mozambique Channel, and with similar bottom slopes) by Konyaev et al. (1995). It has also been studied theoretically by Gerkema (2001) and by Akylas et al. (2007).

The northernmost part of the Mozambique Channel (MC) has been studied by Manders et al. (2004), who showed the existence of ITs (but not ISWs) in the narrowest passage between Mozambique and Madagascar near 15-17 °S. However, to our knowledge, there has so far been no evidence of the existence of ISWs anywhere within the MC, nor of internal tidal activity in the central and southern parts of the MC. In this paper we report recently acquired SAR images of the MC which show for the first time that the Sofala Bank (see Fig. 1) is a “hot-spot” for internal tidal and solitary wave activity. This is in accord with the study of Baines (1982), which estimated energy fluxes from several shelf regions of the world’s oceans, and showed that the MC was amongst the 12 most energetic regions for IT generation. Here, the (semi-diurnal) barotropic tidal ranges are over 7 m, and the barotropic currents typically exceed 50 cm/s at Spring tides, with significant spring-neap variability (see Table 1). The shelf slope is also steeper than the ray paths (see below), allowing the existence of “critical” regions for IT generation. In the present study we show evidence that both the above generation mechanisms are operative in the MC, with waves being formed directly at the shelf break, and remotely through local generation.

The paper is organized as follows. We begin by describing the new satellite SAR observations of the short-period ISW trains in the MC in section 2, together with a preliminary interpretation of their patterns in terms of IT ray propagation pathways. This is followed by an examination of the depth-integrated body force of Baines (1982) in section 3, together with an analysis of cross-slope transports. This is able to explain why the ISWs occur in the observed locations, rather than further north or further south, and confirms the Sofala shelf as a hot-spot region for the ITs and ISWs. The paper then concludes, in section 4, with a more detailed examination and discussion of the SAR observations, the effects of seasonal variations, and the likely generation mechanisms for the ISWs.

2. SAR Observations and Interpretation

It is well known that ISWs propagating on the near surface thermocline (or pycnocline) are capable of producing sea surface roughness patterns that are observable by satellite-borne SARs when the wind speed is not excessively strong (Alpers, 1985; da Silva et al., 1998). Here we investigate available ENVISAT ASAR imagery of the MC region (19-22.5 °S, 34.5-38.5 °E). The ESA EOLI-SA image catalogue was used to analyse quick-looks, and images were then requested when strong signatures of ISWs were visible. Fig. 1 is a composite map derived from six satellite SAR overpasses corresponding to the strongest ISW signatures identified in the ENVISAT images. The images selected were those dated 26 September 2003; 23 April 2004; 10 and 13 August 2005; and 17 and 20 February 2006, and these are identified by different colours in Fig. 1. They all correspond to the Wide Swath WS image mode, which is optimum for observing local generation of ISWs (see da Silva et al., 2007) because of its extensive coverage (400km x 400km) and high spatial resolution (75 m). Although there were additional observations of ISWs in the MC in other satellite datasets (ERS SAR and MODIS), we have not included these because of their smaller swath widths. All the images shown cover the entire area in Fig.1 except for the yellow and red waves (the cutoff for which is at the southern edge of the wave packets shown).

Detailed inspection of the SAR signatures (in the manner of Thompson and Gasparovic, 1986) reveals that the ISW packets shown (having crests approximately parallel to the shelf break) all propagate offshore in the general direction of ESE or SE. The overall pattern of the ISW trains is similar to the patterns previously observed in other regions, such as the Bay of Biscay (New and da Silva, 2002; Azevedo et al., 2006; da Silva et al., 2007). In the northern Bay of Biscay there are enhanced levels of activity close to the shelf break, then an off-shelf region with a reduced number of ISW observations, followed by an increase of activity from about 120-150 km from the shelf break (this latter activity being due to local generation). Similarly, in the MC off the Sofala Bank (Fig. 1), we observe short-wavelength ISW trains near the shelf break (e.g. the 200 m contour), then a decrease in the off-shelf direction, followed by an increase in activity at about 80 km away from the shelf break. This off-shelf region of ISW activity is about 100 km wide, and extends to the SE for some 200 km further offshore towards the centre of the Channel.

We also note in passing that no ISW packets were seen on the shelf, whereas at first sight, one would expect waves to be visible both oceanwards and shelfwards of the shelf break. For instance, Lamb (1994) modelled internal wave generation over Georges Bank and showed that these could propagate both off-bank and onto the bank. However, the stratification used by Lamb had a strong sharp thermocline (with a maximum $N = 0.027 \text{ s}^{-1}$). In the present case, the waters on the Sofala Shelf are essentially well mixed due to the strong tides there (N below 0.003 s^{-1}), and so cannot support the propagation of internal waves (for which stratification is required).

To begin to explain these patterns in more detail, we now turn to theoretical considerations. Internal tides in a continuously stratified ocean can be described by beams or rays that follow characteristic pathways (along which their energy can propagate) with a slope c to the horizontal given by

$$c = \pm \left(\frac{\sigma^2 - f^2}{N^2 - \sigma^2} \right)^{1/2} \quad (1)$$

where N is the local Brunt-Väisälä frequency, σ is the semi-diurnal frequency, and f the Coriolis parameter. When the seafloor slope matches the local value of c (a “critical” region) generation of ITs is pronounced, particularly if the barotropic currents are strong. In such cases, the direction of the forcing barotropic flow is then coincident with the motion plane for free internal waves, resulting in resonant conditions and enhanced generation of the ITs.

Fig. 2a shows average profiles of the Brunt-Väisälä frequency for different seasons and locations in the MC. The dark blue profile represents an average stratification for October 2007 based on 10 CTD stations from close to profile P1 in Fig. 4a (also shown in Fig. 1) and covering water depths between 326 and 2192 m (with a mean latitude of 20.25 °S). The red profile is based on 9 CTD stations from the RV Pelagia (cruise 64PE156) in March 2000 and represents an average stratification of the summer season from a zonal section at 20 °S (water depths between 270-2500 m) close to P1. This latter is very similar to the stratification presented by Manders et al. (2004) for the same month (March) but further north (at 16.5 °S). We have also evaluated an average stratification for November 2007 (the green curve in Figure 2a) in a region close to section labeled P3 in Fig. 4a. The stations used have an average latitude of 17.75 °S, and cover water depths between 300-2200 m. The Brunt-Väisälä frequency profiles are quite similar for both P1 and P3 regions at this time of year, taken as representative of spring stratification. Fig. 2a therefore provides a good description of the variability of the stratification within the MC, both spatially and seasonally.

In Figs. 2b and 2c we present internal tide ray paths computed using the stratifications for March and October, respectively, both for the M2 and S2 tidal frequencies (respectively 1.4052×10^{-4} rad/s and 1.4544×10^{-4} rad/s). The ray paths are computed along the section in Fig. 1 shown by the black line oriented almost perpendicularly to the 200m isobath (that is also coincident with profile P1 in Fig 4a). The rays emanate from the critical region of the shelf break, initially slope downwards into the deep ocean, reflect upwards from the seafloor at a depth of 1100- 1300 m (some 35-45 km seawards from the shelf break), and re-emerge at the surface at about 75-90 km from the break. From one season to another, there is a spatial

(horizontal) difference of about 5-7 km between the positions of the rays when they reach the surface after bottom reflection.

A similar difference arises between the ray positions for the M2 and S2 frequencies for a given season. It is important to acknowledge that the divergence of the ray paths for the M2 and S2 frequencies will mean that baroclinic spring tides at any location will not necessarily occur at the same time as barotropic spring tides. As shown by Gerkema (2002), the time of occurrence of baroclinic spring tides depends spatially on the local phase difference of the M2 and S2 (lunar and solar semi-diurnal) tides. These phases in turn depend on the pathways which the two rays follow. The divergence of the two rays will therefore lead to possible differences in the timing of baroclinic spring tides (i.e. the forcing by the upward beam when it strikes the thermocline in the local generation process will not necessarily be a maximum at the same time as barotropic spring tides at the shelf break). However, we comment that we were only able to find examples of waves in the SAR images within a few days of barotropic spring tides (see Table 1 below), so this effect appears to be small in the present case.

The red star and black square in Fig. 1 show the positions where the ray in Fig. 2c (for October stratification and the M2 frequency) is generated (the “critical” position) and where it subsequently intersects the thermocline (at 60 m depth), respectively. Measured at the surface, a distance of about 80-85 km off the Sofala Bank region is typical for this ray bounce geometry. This is shown in Fig. 1 by the red discontinuous (dash-dot) curve and the black dashed curve. These represent the approximate positions of the critical topography along the shelf break and the intersections of the re-emerging IT rays with the thermocline in the oceanward direction, respectively, and have been drawn from the analysis of several rays similar to that shown in Fig. 2c.

It is clear in Fig. 1 that the ISW packets close to shelf break are generally composed of just a few waves of relatively small wavelength (0.5-1.5 km) when compared to (some of) the wave trains observed further offshore (wavelengths in excess of 5 km). There is a region of relatively low ISW activity between the shelf break and the re-emergence at the surface of the IT rays. This is followed by a marked increase in ISW activity at about 80 km from the shelf

break which coincides closely with the surfacing positions of the IT rays. Consequently, it would seem that at least some of these wave packets could potentially result from local generation. Typically, multiple ISW packets are observed in any particular image, except for those on 26 September 2003, marked orange in Fig. 1 (and in some recent images where only a single soliton was observed, in summer, that are discussed in section 4). In these individual images (e.g. the dark blue waves), the ISW packets are separated by typical distances of 60-70 km. Assuming this is the distance the packets travel between tidal cycles implies a phase speed of 1.35 – 1.55 m/s. This is consistent with phase speeds inferred from the local stratification (two-layer model), and so confirms that the packets do indeed have a tidal origin, and are generated on succeeding tidal cycles (as is typically the case in other areas).

In addition, in the off-shelf region of ISWs in Fig. 1, there are ISW packets with both large and small wavelengths at the same time, and closely located to one another. For instance, in the ISW packets coloured light blue, dark blue and yellow (dated 10 August 2005, 17 February 2006 and 20 February 2006, respectively), there are such wave groups near and oceanwards of the ray surfacing position. The packets of longer waves occur ahead of (further to the SE) the shorter waves. The occurrence of seemingly different types of ISWs also indicates the possibility that these packets could result from different generation mechanisms (i.e. from the shelf break, and locally), and this is investigated further below.

We note that the ISWs which occur during the southern summer generally penetrate further into the Channel than those occurring during the winter. On the other hand, those occurring during the winter are generally found further to the south than those occurring in the summer. Possible reasons for these differences are discussed in section 4.

3. Body Force Modelling

We now examine why the ISWs are seen in the observed locations through an investigation of the barotropic body forcing term for the ITs. This has been found to be a useful indicator of where hot-spot generation regions of ISWs may occur in several other independent

studies (Sherwin et al., 2002; Merrifield and Holloway, 2002; Niwa and Hibiya, 2004; Azevedo et al., 2006; da Silva et al., 2007).

Following Baines (1982), the barotropic forcing term, or “body force”, for internal tides resulting from shelf break interactions, can be found as

$$F = zN^2(z) \int Q dt \cdot \nabla \left(\frac{1}{h} \right) \quad (2)$$

where z is the upward vertical direction, $N(z)$ is the local Brunt-Väisälä frequency, Q is the barotropic mass flux vector $Q = (Q_x, Q_y) = (u_1 h, v_1 h)$, u_1 and v_1 are the zonal and meridional components of the barotropic velocity, and h is the ocean depth. The body force F can thus be analytically integrated provided the mass flux vector Q is known. In the present work, the components of the barotropic velocity vector were obtained from the $1/4^\circ$ resolution (global) tidal model OTIS (Oregon State University Tidal Inversion Software), developed by Egbert and Erofeeva (2002). We first calculated the components of the barotropic mass flux vector (Q_x and Q_y) for a complete tidal cycle (on any particular day) on an interpolated grid with resolution of $1/8^\circ$. The model included the M2 and S2 constituents of the barotropic tide, as these are the most important for determining the conditions at Spring tides for the study region. The model was run for all the dates of the SAR images with strong internal wave events and shown in Fig. 1. The Brunt-Väisälä frequency N was assumed to be spatially constant over the study region (given the small spatial variability discussed in section 2), and we accounted for seasonal differences by using the most appropriate profile for the date of each SAR image (from March or October on the P1 section in Fig. 2a).

Figs. 3a and 3b show the depth-integrated body force for the region of the Sofala Bank (18-23 °S; 35.25-39 °E). For each of the days when there was a satellite overpass, one of these maps was created of the tidal maximum (vertically) integrated forcing for each point of the model domain. Fig. 3a is the average of the three maps corresponding to the individual SAR images of the summer season (taking the average stratification of March). Similarly, Fig. 3b is

the average of the three maps corresponding to the individual SAR images of the spring season (taking the average stratification of October). It can be clearly seen that there is a region of elevated and coherent values of strong forcing along the shelf break and close to the 200 m contour, from approximately (20 °S, 36.4 °E) to (21.3 °S, 35.6 °E), in both Figs. 3a and 3b. In fact, both body-force maps are qualitatively similar, the differences being essentially in the maximum values of integrated body-force which are higher for the summer season, as one would expect since N is also higher (see eq. 2). This region has an average maximum forcing of $5.76 \text{ m}^2 \text{ s}^{-2}$ and $4.56 \text{ m}^2 \text{ s}^{-2}$ for the summer and spring season, respectively (the values for the individual maps corresponding to the days of the individual images are given in Table 1). This is significantly higher than the body-force previously calculated for the southern Bay of Biscay and the southern Iberian regions (Azevedo et al., 2006; da Silva et al., 2007). The Mozambique Channel, and in particular the region off the Sofala shelf, is therefore identified as an efficient generator of baroclinic tides. Moreover, the observed ISW wave trains (overlaid in Figs. 3a and 3b) appear directly oceanwards of the region of maximum body force, in a direction consistent with their propagation direction.

Since tidal elevations of the barotropic tide are large throughout the MC and in fact increase to the north of Sofala Bank, being higher at the narrowest part of the MC (see map of lunar semi-diurnal tidal component M2 based on Topex/Poseidon Altimetry data available at <http://svs.gsfc.nasa.gov/stories/topex/tides.html>), we now extend some of the analysis further north, to cover the region studied by Manders et al. (2004), near 16.5 °S. Figure 4a presents a body-force map, computed in the same manner as described above for a larger region (16-23 °S; 35.25-41 °E), and representing the conditions for 26 September 2003 (orange waves in Fig. 1). This case has the maximum forcing of all examples in winter, when conditions might be most favourable for local generation. One can see from Fig. 4a that the body-force values progressively decrease and become less coherent in space to the north. Since there is very little difference in stratification at various positions along the shelf-slope, this is instead likely to be due to differences in the topography. To better understand this we also show the cross-slope transports in Fig. 4b, computed for three cross slope sections along the western margin of the

MC (P1, P2 and P3). The importance of the cross-slope mass fluxes in determining the energy fluxes in the internal waves which radiate away from the shelf-slope bathymetry has been pointed out by Morozov (1995). It can be seen that cross slope transports are large ($Q=50 \text{ m}^2\text{s}^{-1}$) and comparable to other regions where ISWs are observed (Gerkema et al., 2004) for profile P1 (Sofala) but rather small further north for profiles P2 and P3 (see Fig.s 4a and 4b). Indeed, for steep (supercritical) slopes, such as those off the Sofala Bank, the internal tidal energy flux (equivalent to the integrated conversion rate C_{int} of Gerkema *et al.*, 2004) is actually proportional to the square of the mass (or volume) flux Q , which further enhances the contrast between P1 on the one hand, and P2/3 on the other. This further emphasizes the high efficiency of the Sofala Bank in generating internal tides, as compared to the region previously studied by Manders *et al.* (2004).

Now, the body force (see Azevedo et al., 2006) is related to the product of the topographic slope and the transport crossing this topography. There is not much difference in the topographic slope offshore from the shelf break at depths greater than 100 m (see Fig. 1). However, the cross-slope transport is very large for the section P1 passing through the region of the body force maximum, and is much smaller at locations (P2 and P3) further along the shelf slope. In turn, we anticipate that this cross-slope transport is so large here because of the detailed nature of the topography. In particular, there are two raised banks, less than 50 m depth, at 20.6° and 20.4°S . The barotropic tide is forced around and between these two banks, and moreover is allowed to flow without hindrance onto the broad shelf area further to the east, being further encouraged to do so by the area deeper than 50 m directly behind these banks. This is similar to the situation on the Hawaiian island chain in which the topographic forcing is much enhanced at the saddle points between the islands, giving rise to regions of large internal tidal energy fluxes there (e.g. Merrifield and Holloway, 2002). Thus we believe that the special form of the shelf break topography near 20.5°S gives rise to the strongest cross-slope transports, and so to the strongest body force, and hence to the preferred generation of the ISWs from this location. Further north as the shelf becomes progressively narrower, it becomes increasingly hard for the barotropic tide to flow across the shelf-slope and into such a reduced

shelf area. The tidal ellipses become preferentially aligned in the along-slope direction. Thus in the region covered by Manders et al. (2004), the generation of ITs is weaker and no ISWs were observed by these authors in this location (and neither in the SAR images used in our study).

We therefore conclude that the ISWs observed in the SAR images do indeed result from the forcing due to the interaction of the barotropic tides with the shelf break topography, and are found directly oceanwards of the region of maximum forcing, as would be expected. This shows that the body force is indeed a good indicator of where the waves are most likely to be observed, and supports our choice in using it. It also appears that the body force must reach a certain value before the waves will appear, as no waves are seen further along the shelf slope where the body force is weaker.

4. Discussion

We now discuss in more detail the SAR signatures of the ISWs and make suggestions as to possible generation mechanisms. Fig. 5 is an extract of the ENVISAT ASAR image from 17 February 2006 (waves marked in dark blue in Fig. 1) corresponding to an area of approximately 155 x 95 km. Several individual wave packets can be identified. Starting from the left, there is an ISW packet (A) of relatively short wavelengths near the shelf break. This contains at least 8 well-developed waves with typical wavelengths of about 1 km. Some 67 km further to the ESE, in the general propagation direction of the ISW trains, we observe another wave train labelled B. The wavelengths in packet B are considerably larger (2 to 3 km) than for packet A, and there are at least 20 waves with typical along crest distances of 100 km. Further offshore (in the direction of ISW propagation), another wave packet (C) is found 63 km away from B. The inter-packet separations between packets A and B, and B and C, are typical of internal tide wavelengths, and correspond to an average phase speed of approximately 1.4-1.5 m/s (the long wave speed for a two layer model using appropriate parameters for the study region is close to this, being approximately 1.4 m/s).

However, in between packets B and C we note the presence of another large-scale wave packet, labelled D in Fig. 5. The wavelengths of packet D (distance between wave crests) are considerably larger (7-3 km) than those for packets B and C, possibly indicating a different generation mechanism. The discrepancy between the wavelengths in packets D and B is further illustrated in Fig. 6 which provides a SAR image intensity profile across packets D and B in the region denoted by the white rectangle in Fig. 5. We interpret packet D as containing the leading three longest waves on the right-hand side of the figure, which is followed by packet B. Packet D is therefore approximately 15 km in length overall, and contains waves with separations rank ordered as 7, 5 and 3 km. Furthermore, the intensity profile in Fig. 6, taken as the relative variation compared to the unperturbed mean backscatter (see da Silva et al., 1998, for more details) decreases from the front to the rear of Packet D (from 1.8 to about 0.05 units for the crest values), but then rises again (to 1.5 units) for Packet B. These intensity variations are related to the amplitudes of the underlying ISWs (i.e. to the displacements of the isopycnals), although their inter-relationship is not straightforward because of other factors (such as the wind speed and direction, and the presence of surface films). Nevertheless, because of the non-monotonic variation of the SAR image intensity and taking into account the disparity between the wavelengths from packets D and B, we suggest that these are two individual wave packets which are likely to have different generation mechanisms.

We therefore propose that packet B was formed a (semi-diurnal) tidal cycle before packet A at the shelf break, and propagated from its origin for a tidal wavelength (67 km) to reach the observed position. We also interpret packet C as the predecessor of packet B since this is located a further 63 km offshore. At an additional 60 km offshore in the same direction (towards the ESE) there is another packet (not shown in Fig. 5, but indicated, and also shown in dark blue in Fig. 1) that therefore also appears to be part of the same family (i.e. with the same generation site and mechanism). We note that the above mentioned wave packets are approximately equally spaced (67, 63, 60 km apart), although their inter-packet separation decreases oceanwards. Also, the wave crest separation within packet C seems to be slightly larger than in the packet further offshore (see dark blue waves in Fig. 1). This latter aspect

seems at first contrary to what should be expected from nonlinear theory of solitary wave propagation, as the individual waves should spread apart along their offshore propagation direction into deeper waters. However, analysis of MODIS Ocean Color level 3 images and Sea Surface Height Anomalies of Topex/Poseidon (not shown) revealed the presence of a large anti-cyclonic eddy in the locality of these wave packets which would impose an adverse current against wave packets C and that further offshore (the eddy being centered at 38 °E, 23 °S and with an northern edge near 21 °S). It is likely that this would act (through internal wave-current interaction) to reduce the wavelengths of the individual waves in the most offshore wave packet, as well as reducing the inter-packet spacings between packets B and C, and between packets C and that further offshore. Similar effects on ISWs have been observed by Sabinin and Serebryanyi (2007). Overall, we therefore interpret these wave packets (A, B, C and that further offshore) as resulting from direct generation at the shelf break on successive tidal cycles.

However, it seems unreasonable to include packet D in the same grouping. For if we supposed that packet D was actually the leading edge of the first wave group oceanwards from the shelf break (instead of packet B), this would lead to inter-packet spacings of 82, 48, and 60 km. These would not form a regular series and so we discount this possibility. We thus hypothesise that packet D is an independent wave packet, with a different generation mechanism. The location of packet D is consistent with the local generation hypothesis, in that it is found just to the oceanward side of the emerging IT wave beam in Fig. 1. The emerging IT wave beam, after reflecting from the sea floor, impinges on the thermocline from below at 20.9 °S, 36.54 °E, some 20 km from the leading wave in packet D. This geometry is similar to those previously observed in the Bay of Biscay and off the Iberian shelf, in which the locally-generated ISW trains are first observed 20 -30 km away (in the direction of ray propagation) from the position of the ray intersection with the thermocline. (This gives time for the ISWs to form from the large IT displacements of the thermocline there.)

Furthermore, in Fig. 7 we show another example of a SAR image (that from 20 February 2006) with two distinct ISW packets, labelled E and F (these are also shown in yellow in Fig. 1). Packet E, the wave train further offshore, has two clear large-scale wave crests that

show as bright bands on a dark background (this type of SAR signature is typical of very low wind speeds, as has been explained by da Silva et al., 2000). Shelfwards of packet E we see another wave packet labelled F. This is characterized by much shorter waves (with an average wavelength of 1.5 km as compared with 5 km for packet E). As can be seen both here and in Fig. 1, packets E and F are propagating in rather different directions (packet E towards 140° T and packet F towards 120° T) and have the appearance of being completely separate wavetrains. Moreover, packet E is oceanward of the surfacing of the IT ray (see Fig. 1), similarly to packet D in Fig. 5. Since packet F is shelfwards of the IT ray surfacing position while packet E is oceanward of this position we suggest that packet E also results from the local generation mechanism, while packet F is generated at the shelf break.

Several of the other SAR images also show evidence for local generation. For instance, the images from 10 and 13 August 2005 (light blue and red in Fig. 1, respectively) also show large wavelength ISW packets that are consistent (in terms of their location) with local generation. In particular, on 10 August, two sets of ISWs are again apparent near to the ray surfacing position, with the packet of longer waves leading the packet of shorter waves. This again suggests that waves generated both through the local generation process, and from the shelf break, are apparent in this image. In addition, on 26 September 2003, the only ISW packet observed (the orange waves in Fig. 1) are of long wavelength (matching the wavelengths of the other packets identified as being locally generated), and there are no other wave packets closer to the shelf break (as would be expected if the waves were generated tidally at the shelf break). Consequently, it seems that only local generation may be occurring on this occasion.

Table 1 now summarises properties of the waves identified as having been locally generated. For each of the six SAR images discussed, the table presents the maximum depth-integrated body force, the tidal range on the day in question (high-low water difference at the coastline in Beira, 20° S), the spring-neap tidal range for the time period spanning the observation date, the number of solitons identified as locally generated, and their “widths” defined from the SAR transects (this latter quantity being the width over which the SAR backscatter rises significantly above the background value). (This latter quantity is not the same

as the wavelengths previously referred to, and refers to the average width of the leading soliton in the packet in question.) The locally generated waves generally have larger wavelengths and are wider than those emanating from the shelf break. Their widths vary between 1.4 and 2.6 km. Table 1 also shows that we were only able to find examples of waves in the SAR images within a few days of barotropic Spring tides at the shelf break (i.e. the tidal range on the day in question is always close to the range of the neighbouring Spring tide). Although Gerkema (2002) showed that baroclinic spring tides may have an appreciable phase shift from the time of barotropic spring tides, this appears to be a relatively small effect here, as discussed earlier.

We now discuss the effects of the seasonal variation of the stratification on the ISWs. Firstly, we note that there are appreciable differences between the wave packets in the southern summer (February-April, being further north and extending further into the channel) and those in the southern winter (August-September, being further south and extending less far into the channel). We have investigated the seasonal variation in stratification in Fig. 2a and shown that the main difference between the seasons is that the stratification is stronger during the southern summer within the seasonal thermocline (depths shallower than 100m). This means both that the ray paths penetrate more extensively into the channel at this time of year, and that the body force (thought to generate the waves, and proportional to N^2) is stronger. However, the surfacing positions of the rays are only different by about 5 km, and so unlikely to explain the deeper penetration of the waves into the channel (by 50-100 km). Furthermore, a simple two-layer calculation shows that the long wave phase speed is about the same (1.4 m s^{-1}) at both times of year (the weaker thermocline in October being compensated by a deeper upper layer), so that seasonal differences in the wave speeds must also be discounted from any explanation of deeper penetration into the channel during the southern summer.

However, we have shown that the average of the maximum depth-integrated body force is $5.76 \text{ m}^2\text{s}^{-2}$ in March but only $4.56 \text{ m}^2\text{s}^{-2}$ in October. We feel that this stronger body force offers a more plausible explanation of why the waves penetrate further into the channel at this time of year (i.e. during the southern summer when the body force is stronger, and the waves would be expected to be more energetic). Another possible factor for the more extensive

penetration of the waves into the channel in the southern summer is that the thermocline at this time of year may sustain any generated interfacial waves better than the thermocline in the winter. The rate at which wave energy would leak from the thermocline into the deeper ocean (causing dissipation of the waves on the thermocline) has been termed “radiation damping” and investigated theoretically by Ayklas et al. (2007). Given that the long wave speeds (c_0) are similar for both the present stratifications (as mentioned above), but that the upper layer depth (h) is larger in October (see figure 2a), then the parameter μ of Ayklas et al. (2007) will be larger in October (i.e. in the winter/spring), with more rapid dissipation of the waves being expected (see equations 2.3 and 2.18 of Ayklas et al., 2007).

Turning now to the issue of why the waves are further to the south in the southern winter, we consider the seasonal variation of the currents in the region. While Schott and McCreary (2001) indicate that there seems to be insufficient observational evidence to make reliable statements about variations in the currents in this region, Maltrud et al. (1998) offer insights from a high resolution modeling study with the POP model. This shows that the Mozambique Current (which flows southwards along the western slopes of the basin) is much stronger during July-September (often 10-15 Sv southwards) than during March-May (typically 0-5 Sv southwards). We believe that the increased southward flow in the southern winter months would be likely to refract (advect) the waves towards a more southerly pathway at this time of year, as observed.

We next consider the effect of seasonal variations in the stratification on the “local generation” process. In an idealized modeling study, Gerkema (2001) showed that this would only occur for thermoclines of “intermediate” strength, for which the reduced gravity parameter g' (for a two-layer stratification) lay between 0.002 and 0.02. We have estimated this parameter for the present study area as $g'=0.035$ for October and $g'=0.042$ for March. While these values are somewhat higher than Gerkema’s theoretical “intermediate” range, they are significantly lower than other ocean basins (e.g. 0.08 in the Sulu Sea), and than Gerkema’s “strong” thermocline case ($g' = 0.4$). Hence while we believe (from the examples presented here) that local generation is possible for both these values of g' , it may be that the winter stratification

with the lower value of g' is more conducive to local generation. This may also be inferred from the separate modelling study of Akylas et al. (2007), who investigated local generation when a beam of tidal energy is incident on the thermocline from below. For a tidal beam of fixed amplitude ($C=1$), we may compare their figs 6a, for a strong thermocline (with normalised density jump $\Delta = 4 \times 10^{-3}$ across the thermocline, and only few locally generated solitons), fig. 4b (intermediate thermocline, $\Delta = 1.5 \times 10^{-3}$, many solitons), and fig. 6b (weak thermocline, $\Delta = 0.04 \times 10^{-3}$, fewer solitons again). For the present case, our value of Δ is 4.2×10^{-3} in the summer and 3.5×10^{-3} in the winter, thus indicating that our winter examples would be expected to show more locally generated solitons.

This conclusion is indeed borne out by the observations, as shown in Table 1. Our images during the winter typically have 4-6 locally generated solitons, whereas those in the summer have less than (or equal to) 3. We have also identified three additional ENVISAT SAR images (dated 20 May 2007, 22 February 2008 and 24 February 2008, not shown), which show only one large (in terms of width) solitary wave off the Sofala Bank, at distances consistent with local generation. These images correspond to the summer season, when the thermocline strength is enhanced. This supports our conclusion that local generation is more likely in the winter months.

Finally, diurnal tides can propagate as free waves in the region north of 30° S, and so could be potentially important in the Mozambique Channel. However, Egbert and Ray (2003) computed (from T/P data) tidal dissipation rates and vertically integrated kinetic energy global maps for diurnal and semi-diurnal constituents. Their results (figures 1 and 2) suggest that, in the Mozambique Channel, barotropic to baroclinic conversion (i.e. the generation of internal tides from surface tides) is much stronger for semi-diurnal tides (M_2) than for diurnal tides (K_1). In addition, ray tracing diagrams show that diurnal frequency IT beams would re-emerge at the surface at about 230 km from the shelf break, much too far to play a part in explaining the occurrence of the observed ISWs from about 80-90 km from the shelf break. We thus conclude that, in the Mozambique Channel, diurnal tides are not expected to play an important role in the generation of internal tides and ISWs.

In conclusion, we have identified the Mozambique Channel, and in particular the Sofala Shelf between 20-21 °S, as a “hot-spot” for the generation of internal waves and internal tides which travel oceanwards away from the shelf break. This results from a strong barotropic tidal forcing and large cross-slope transports, coupled with shelf break topography that is sufficiently steep for critical regions to occur from which deep oceanward internal tidal rays may emanate. The hotspot region is localised between 20-21 °S because of the particular nature of the bathymetry there. Further north and south, the forcing is reduced and insufficient to generate ISWs. We have suggested that the internal solitary wave packets result from both direct generation at the shelf break, and from local generation at about 80 km oceanwards from the break due to the surfacing of internal tidal rays at the thermocline. Finally, we have investigated seasonal differences in the wave patterns, which penetrate more extensively into the channel during the southern summer, and appear slightly further to the south during the southern winter. We also conclude that the local generation process is more likely to occur during the winter when the stratification is reduced.

Acknowledgements.

The SAR image data presented here were provided by the European Space Agency (ESA) under project number AOPT-2423. The work was undertaken as part of the SPOTIWAVE-II – Hot-Spots of internal wave activity off Iberia revealed by multi-sensor remote sensing satellite observations (project codes POCI/MAR/57836/2004 and POCTI/CTA/41130/2001) and AMAZING (project code PDCTE/CTA/49953/2003) projects, funded by the Portuguese Science and Technology Foundation (FCT). We thank both the reviewers for their helpful comments, which we feel have helped to improve the paper significantly.

References

Alpers, W. (1985), Theory of radar imaging of internal waves, *Nature*, 314, 245-247.

Akylas, T.R., R.H.J. Grimshaw, S.R. Clarke, and A. Tabaei (2007), Reflecting tidal wave beams and local generation of solitary waves in the ocean thermocline, *J. Fluid Mech.*, 593, 297-313, doi:10.1017/S0022112007008786.

Azevedo, A., J.C.B. da Silva, and A.L. New (2006), On the generation and propagation of internal solitary waves in the southern Bay of Biscay, *Deep Sea Res. I*, 53, 927-941.

Baines, P.G. (1982), On internal tide generation models, *Deep Sea Res.*, 29, 307-338.

da Silva, J.C.B., S.A. Ermakov, I.S. Robinson, D.R.G. Jeans, and S.V. Kijashko (1998), Role of surface films in ERS SAR signatures of internal waves on the shelf. I. Short-period internal waves, *J. Geophys. Res.*, 103 (C4), 8009-8031.

da Silva, J.C.B., S.A. Ermakov, I.S. Robinson (2000), Role of surface films in ERS SAR signatures of internal waves on the shelf. III. Mode transitions, *J. Geophys Res.*, 105 (C10), 24089-24104, doi: 10.1029/2000JC900053.

da Silva, J.C.B., A.L. New, and A. Azevedo (2007), On the role of SAR for observing local generation of internal solitary waves off the Iberian Peninsula, *Can. J. Remote Sens.*, 33 (5), 388-403.

Egbert, G.D., and S.Y. Erofeeva (2002), Efficient inverse modeling of barotropic ocean tides, *Journal of Oceanic and Atmospheric Technology*, 19, 183-204.

Egbert, G. D., and R. D. Ray (2003), Semi-diurnal and diurnal tidal dissipation from TOPEX/Poseidon altimetry, *Geophys. Res. Lett.*, 30(17), 1907, doi:10.1029/2003GL017676.

Garrett, C., and L. St. Laurent (2002), Aspects of Deep Ocean Mixing, *J. Oceanogr.*, 58, 11-24.

Gerkema, T. (2001), Internal and interfacial tides: beam scattering and local generation of solitary waves, *J. Mar. Res.*, 59, 227-255.

Gerkema, T. (2002), Application of an internal tide generation model to baroclinic spring-neap cycles, *J. Geophys. Res.*, 107(C9), 3124, doi:10.1029/2001JC001177.

Gerkema, T., F-P.A. Lam, and L.R.M. Maas (2004), Internal tides in the Bay of Biscay: conversion rates and seasonal effects, *Deep Sea Res. II*, 51, 2995-3008.

Konyaev, K.V., K.D. Sabinin, and A.N. Serebryany (1995), Large-amplitude internal waves at the Mascarene ridge in the Indian Ocean, *Deep Sea Res. I*, 42, 2075-2091.

Lamb, K.G. (1994), Numerical experiments of internal wave generation by strong tidal flow across a finite amplitude bank edge, *J. Geophys. Res.*, 99 (C1), 843-864.

Maltrud, M.E., R.D. Smith, A.J. Semtner, and R.C. Malone (1998), Global eddy-resolving ocean simulations driven by 1985-1995 atmospheric winds, *J. Geophys. Res.*, 103 (C13), 30825-30853.

Manders, A.M.M., L.R.M. Maas, and T. Gerkema (2004), Observations of internal tides in the Mozambique Channel, *J. Geophys. Res.*, 109, C12024, doi:10.1029/2003JC002187.

Merrifield, M.A., and P.E. Holloway (2002), Model estimates of M2 internal tide energetics at the Hawaiian Ridge, *J. Geophys. Res.*, 107 (C8), 3179, doi: 10.1029/2001JC000996.

Morozov, E.G. (1995), Semidiurnal internal wave global field, *Deep Sea Res. I*, 42, 135-148.

Moum, J.N., D.M. Farmer, W.D. Smyth, L. Armi, and S. Vagle (2003), Structure and generation of turbulence at interfaces strained by internal solitary waves propagating shoreward over the continental shelf, *J. Phys. Oceanogr.*, 33, 2093-2112.

New, A. L., S. G. Alderson, D. A. Smeed, and K. L. Stansfield (2007), On the circulation of water masses across the Mascarene Plateau in the South Indian Ocean, *Deep Sea Res. I*, 54, 42-74, doi:10.1016/j.dsr.2006.08.016.

New, A.L., and J.C.B. Da Silva (2002), Remote-sensing evidence for the local generation of internal soliton packets in the central Bay of Biscay, *Deep Sea Res. I*, 49, 915-934.

New, A.L., and R.D. Pingree (1990), Large-amplitude internal soliton packets in the central Bay of Biscay, *Deep Sea Res.*, 37, 513-524.

New, A.L., and R.D. Pingree (1992), Local generation of internal soliton packets in the central Bay of Biscay, *Deep Sea Res.*, 39, 1521-1534.

New, A.L., and R.D. Pingree (2000), An intercomparison of internal solitary waves in the Bay of Biscay and resulting from Korteweg-de Vries-type theory, *Prog. Oceanogr.*, 45, 1-38.

Niwa, Y., and T. Hibiya (2004), Three dimensional numerical simulation of M2 internal tides in the East China Sea, *J. Geophys. Res.*, 109, C04027, doi:10.1029/2003JC001923.

Pingree, R.D., G.T. Mardell, and A.L. New (1986), Propagation of internal tides from the upper slopes of the Bay of Biscay, *Nature*, 321, 154-158.

Pingree, R.D., and A.L. New (1989), Downward propagation of internal tidal energy into the Bay of Biscay, *Deep Sea Res.*, *36*, 735-758.

Pingree, R.D., and A.L. New (1991), Abyssal penetration and bottom reflection of internal tidal energy in the Bay of Biscay, *J. Phys. Oceanogr.*, *21*, 28-39.

Pinkel, R. (2000), Internal solitary waves in the warm pool of the western equatorial Pacific, *J. Phys. Oceanogr.*, *30*, 2906-2926.

Schott, F.A., and J.P. McCreary (2001), The monsoon circulation of the Indian Ocean, *Prog. Oceanogr.*, *51*, 1-123.

Sabinin, K.D., and A.N. Serebryanyi (2007), "Hot Spots" in the field of internal waves in the ocean, *Acoustical Physics*, *53*, 357-380.

Sherwin, T.J., V.I. Vlasenko, N. Stashchuk, D.R.G. Jeans, and B. Jones (2002), Along-slope generation as an explanation for some unusually large internal tides, *Deep Sea Res. I*, *49*, 1787-1799.

Thompson, D.R., and R.F. Gasparovic (1986), Intensity modulation in SAR images of internal waves, *Nature*, *320*, 345-348.

Zhao, Z., V. Klemas, Q. Zheng, and X. Yan (2004), Remote sensing evidence for the baroclinic tide origin of internal solitary waves in the northeastern South China Sea, *Geophys. Res. Lett.*, *31*, L06302, doi:10.1029/2003GL019077.

Figure Captions

Table 1. Maximum depth-integrated body force values for all case studies are shown together with the corresponding tidal ranges, the nearest spring-neap tidal ranges, the number of “locally generated” large waves in a packet, and the soliton width (for the first wave in each packet).

Figure 1. Composite map of ISW observations based on ENVISAT ASAR observations from: 26 September 2003 acquired at 7:04 (orange); 23 April 2004 at 7:04 (green); 10 August 2005 at 7:07 (light blue); 13 August 2005 at 7:12 (red); 17 February 2006 at 7:03 (dark blue) and 20 February 2006 at 7:09 (yellow). All times refer to UTC. The straight continuous black line shows the section for the internal tidal ray paths in Figs. 2b and 2c (also P1 in Fig. 4a). The red star marks the position of critical topography for the M2 (October) ray, and the black square its re-emergence at the thermocline. The red dash-dotted line represents the approximate position of critical topography, and the black dashed line the location of re-emergence at the thermocline, for all such rays (see text for details). Contours mark isobaths in meters, and the inset shows the study region in relation to the African continent and Madagascar.

Figure 2. a) Mean stratifications for the study area are shown for October and November (blue and green representative of spring season), and March (red representative of summer season). Stratifications for October and November were computed using sections in the approximate cross-slope direction near P1 and P3, respectively (see Fig. 4a). March stratification was calculated with a zonal section near P1 (see Fig. 4a).

Figure 2. b) Internal tidal ray-tracing diagrams for the M2 (solid line) and S2 (dashed line) tidal constituents assuming the average summer stratification in Fig. 2a. The location of the vertical section is the straight continuous black line in Fig. 1 (also profile P1 in Fig. 4a, see text for details).

Figure 2. c) Same as Fig. 2b but assuming the average spring (October) stratification in Fig. 2a.

Figure 3. a) Map of the average of the maximum depth-integrated barotropic body force for the three summer case studies (23 April 2004, 17 February 2006, and 20 February 2006). Also marked are all the ISW trains from Fig. 1 (dark thin curves). Note the region of strong forcing near the shelf break off Sofala Bank between 20-21 °S. Contours mark isobaths in meters.

Figure 3. b) Same as Fig. 3a for the three winter case studies (26 September 2003, 10 August 2005 and 13 August 2005). Also marked are all the ISW trains from Fig. 1 (dark thin curves). Note the region of strong forcing near the shelf break off Sofala Bank between 20-21 °S. Contours mark isobaths in meters.

Figure 4. a) Extended map of the maximum depth-integrated barotropic body force for 26 September 2003 (16-23 °S; 35.25-41 °E) is shown together with all the ISW trains from Fig. 1 (dark thin curves). Three profiles labelled P1, P2, and P3 (solid black lines) are also marked in the approximate cross-slope direction. Contours mark isobaths in meters.

Figure 4. b) Cross slope transports for the three profiles shown in Fig. 4a (P1, P2 and P3). The red stars mark the positions of critical topography for each corresponding profile. The 200 m and 1000 m depths are also marked by vertical black ticks for each profile. Distances taken in the offshore direction along the marked profiles in Fig. 4a.

Figure 5. Extract of an ENVISAT ASAR image (WS mode) from 17 February 2006 acquired at 7:03 UTC (wave trains corresponding to the dark blue lines in Fig. 1). Four ISW trains can be identified and are labelled as packets A, B, C and D (see text for details). The separations between the various packets are shown in km.

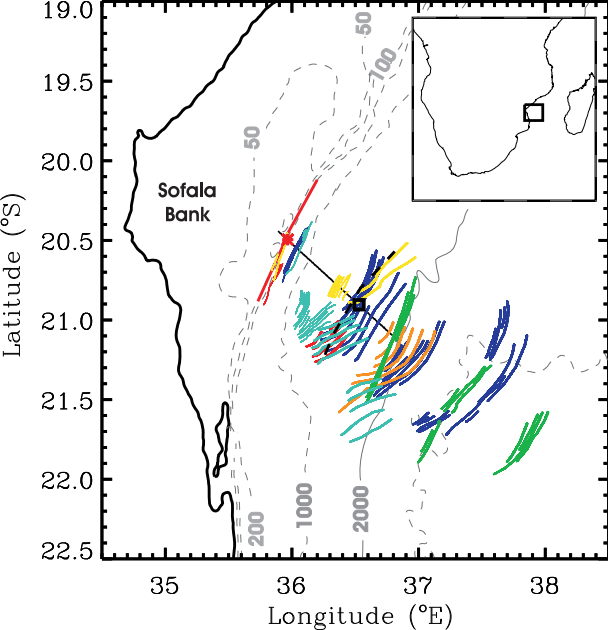
Figure 6. ENVISAT ASAR image intensity profile corresponding to wave packet D and the first five waves of packet B from 17 February 2006 (taken from the white rectangle in Fig. 5).

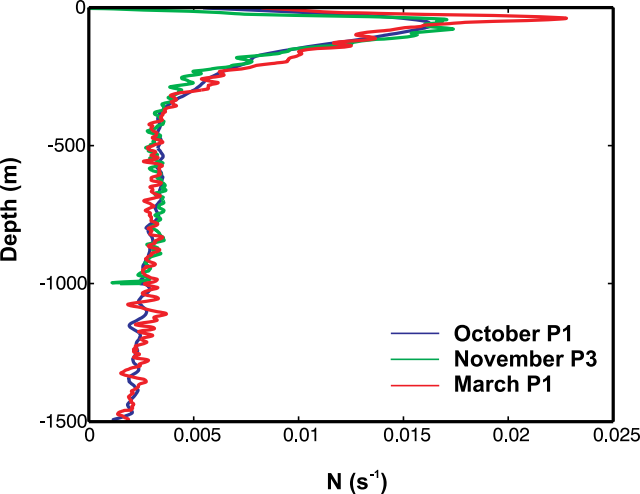
The waves in packet D have wavelengths of 7-3km, whereas those in packet B are shorter than 3 km.

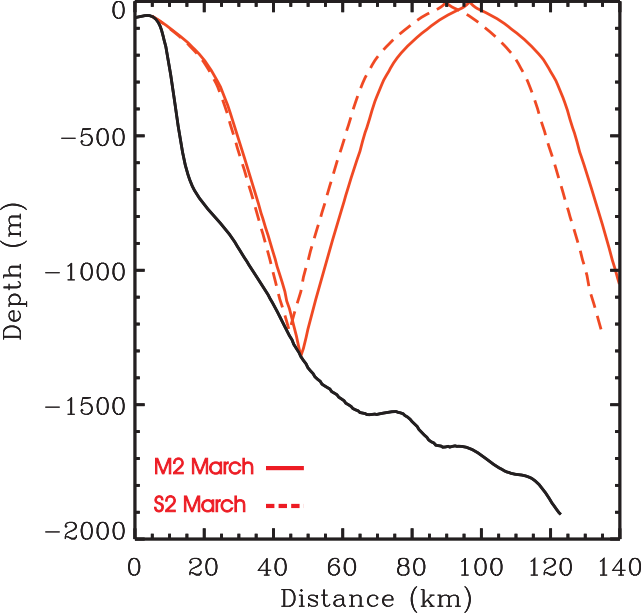
Figure 7. Extract at full resolution of an ENVISAT ASAR image (WS mode) from 20 February 2006 (yellow waves in Fig. 1) showing two distinct wave packets (E and F). The image size is 38 km x 38 km and its centre is at (20.72 °S, 36.48 °E).

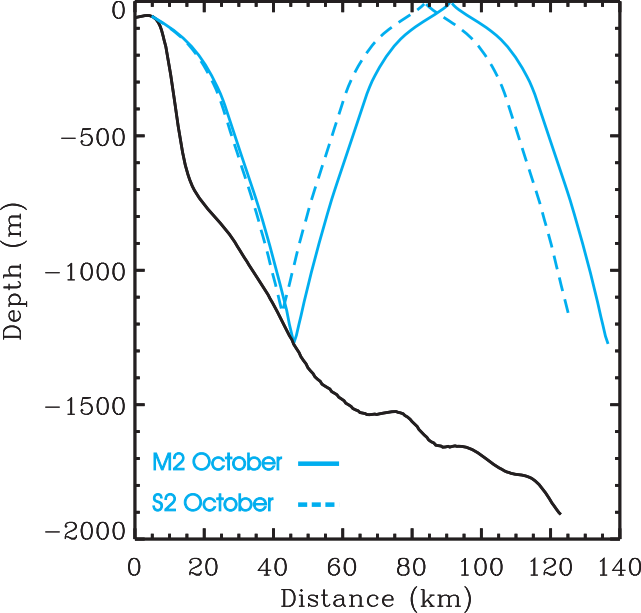
Table 1.

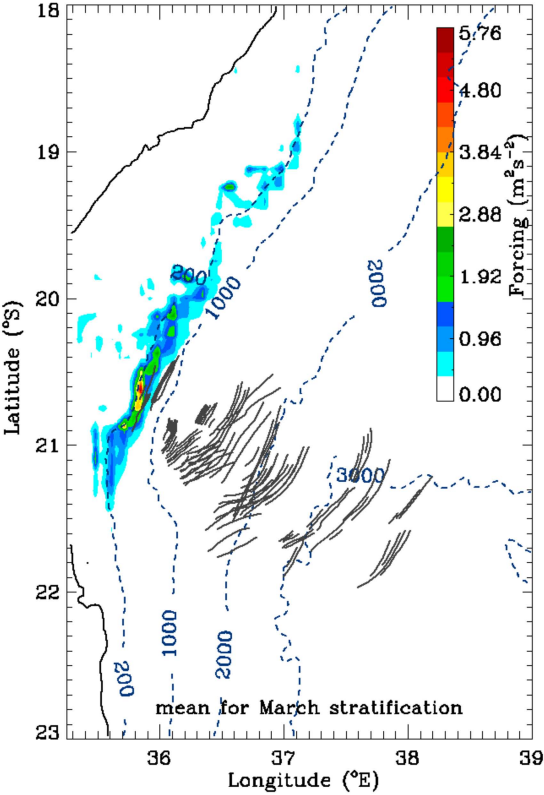
| Date | Maximum Body Forcing (m^2s^{-2}) | Tidal range (m) | Spring/Neap tidal range (m) | Number of locally generated large waves | Soliton width in km (1 st wave in packet) |
|-----------|--|-----------------|-----------------------------|---|--|
| 26Sep2003 | 6.62 | 6.1 | 6.6-1.0 | 6 | 2.6 |
| 10Aug2005 | 5.27 | 4.8 | 4.9-2.1 | 5 | 2.1 |
| 13Aug2005 | 1.80 | 3.4 | 4.9-2.1 | 4 | 2.5 |
| 17Feb2006 | 7.36 | 5.3 | 5.6-1.2 | 3 | 1.4 |
| 23Apr2004 | 6.78 | 4.7 | 5.6-1.0 | 0 | -- |
| 20Feb2006 | 3.14 | 3.8 | 5.6-1.2 | 2 | 1.5 |

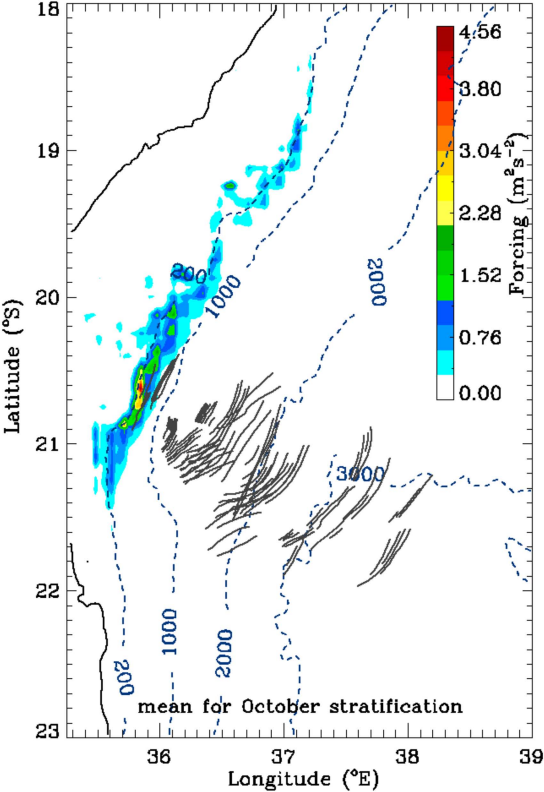


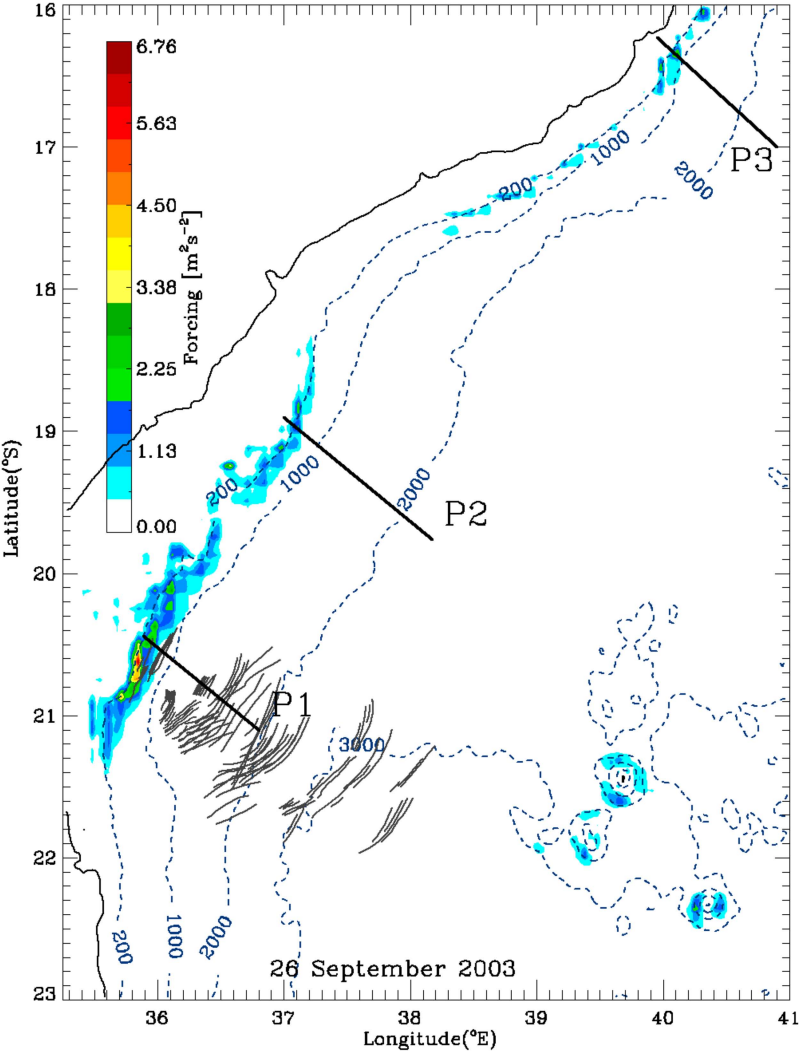












Cross Slope Transports

26 September 2003

